Determining Relation between Size of Polarized Inductive Couplers and Nominal Airgap

Bandyopadhyay, Soumya; Dong, Jianning; Ramirez-Elizondo, Laura; Bauer, Pavol

DOI
10.1109/EPEPEMC.2018.8521895

Publication date
2018

Document Version
Final published version

Published in
2018 IEEE 18th International Conference on Power Electronics and Motion Control (PEMC)

Determining Relation between Size of Polarized Inductive Couplers and Nominal Airgap

Soumya Bandyopadhyay*, Jianning Dong*, Laura Ramirez-Elizondo*, and Pavol Bauer*
*Dept. Electrical Sustainable Energy, DCE&S group
TU Delft, Meklweg 04, 2628 CD, Delft, the Netherlands
Email: s.bandyopadhyay-1@tudelft.nl, j.dong-4@tudelft.nl, l.m.ramirezelizondo@tudelft.nl, and p.bauer@tudelft.nl

***Abstract*—Inductive power transfer (IPT) is gaining popularity across a wide range of battery charging applications like bio-medical, consumer electronics and electric vehicle (EV) charging. One of the major challenges in designing IPT charge pads is determining the optimal physical sizes of the magnetic couplers resulting in efficient power transfer and low cost of materials. In EV applications, it is especially difficult due to the variation in nominal air gap, required power levels associated with different vehicle classes, and charging locations that may be encountered. This paper aims to determine the relationship between optimal coupler sizes and the nominal air gap of an IPT system. Finite element analysis (FEA) is used to model the electromagnetic behavior of the magnetic couplers. A multi-objective optimization framework is built to reveal the Pareto fronts which show the trade-offs between the power transfer efficiencies and the coupler power densities at different air gaps. This method is applied on polarized double-D (DD) couplers for a 5 kW IPT system at different air gaps. Analyzing the power densities of the Pareto Optimal designs an approximate relation between optimal pad sizes and the air gap is derived. Results show that there is an exponential relationship between the optimal coupler sizes and the nominal air gap.**

I. Introduction

Inductive power transfer (IPT) is increasingly used in a wide range of battery charging applications, ranging from low power applications like bio-medical implants [1], consumer electronics to high power applications like industrial automation, and electric vehicles (EVs). EV charging with IPT is more user-friendly than conventional wired charging due to the absence of electrical or mechanical contacts. Additionally, IPT system can be used for in-motion charging of EVs which will reduce range anxiety associated with limited battery capacity. Due to the air gap between the charge pads, there is inherent galvanic isolation between the grid and the EV battery which ensures a spark-free operation minimizing safety concerns. Also, the absence of electrical or mechanical contacts make IPT systems very reliable and virtually maintenance free. Due to these above advantages, IPT technology is a crucial enabling factor for a further increase in the popularity of EVs.

A typical IPT lumped charge pad consists of litze wire for carrying the high-frequency current, ferrites for shaping the flux to improve coupling (k) and aluminum for shielding purposes. Due to the use of expensive materials, it is important to size the pads optimally to reduce the overall system cost while satisfying performance requirements. One of the design challenges in lumped IPT systems is determining the physical sizes of the IPT couplers. This is mainly due to variations of airgap due to different vehicle classes and charging locations. These airgap variations can lead to differing power transfer efficiencies due to the different levels of coupling between the primary and secondary pads. For example, a pair of IPT couplers will transfer the same power at lower efficiency when the nominal air gap is increased. Pad sizing deals with sizing the charge pads so that the desired power transfer efficiencies are achieved within the constraints or defined specifications. Misalignment operating conditions can also affect the optimal size of IPT pads [2]. There are a few reported literature on pad sizing for IPT EV applications [3], [4]. A ball-park approach was proposed in [3] for sizing of charge pads on various vehicle classes. The main result reported was that lowering airgaps for SUVs and trucks can drastically reduce the size and thereby cost of the pads and overall IPT infrastructure. However, the designed charge pads were not optimized and detailed coil losses were not considered. Therefore, derivation of scaling laws between sizing and nominal airgap was not possible. To that end, the goal of this paper is to derive scaling laws for IPT charge pads with a varying nominal airgap.

This paper utilizes a multi-objective optimization approach introduced in [5], [6] to reveal the design trade-offs between efficiency (η), pad area (α) and pad weight (ω) at different airgaps regarding Pareto fronts. The Pareto fronts of the optimization targets are then compared at different airgap to analyze the scaling behaviour of couplers. Polarized couplers [7], [8] also known as double-D (DD) are used as a case study. A 3D finite element (FE) modeling is employed combined with analytical loss equations to model the loss mechanisms in the coil structure.

The paper is structured into six sections. The paper begins by introducing the fundamental theory behind IPT and identifies the important performance metrics. Section III is about the modeling strategy of the IPT coils and the associated loss mechanisms. The multi-objective optimization strategy including the optimization algorithm, targets and the design space is discussed in detail in Section IV. The optimization results are also discussed in detail in the following section. Section V also derive the scaling laws for IPT sizes with the nominal air gap. Finally, the summary along with general conclusions and future work are discussed in the section VI.

978-1-5386-4198-9/18/$31.00 ©2018 IEEE

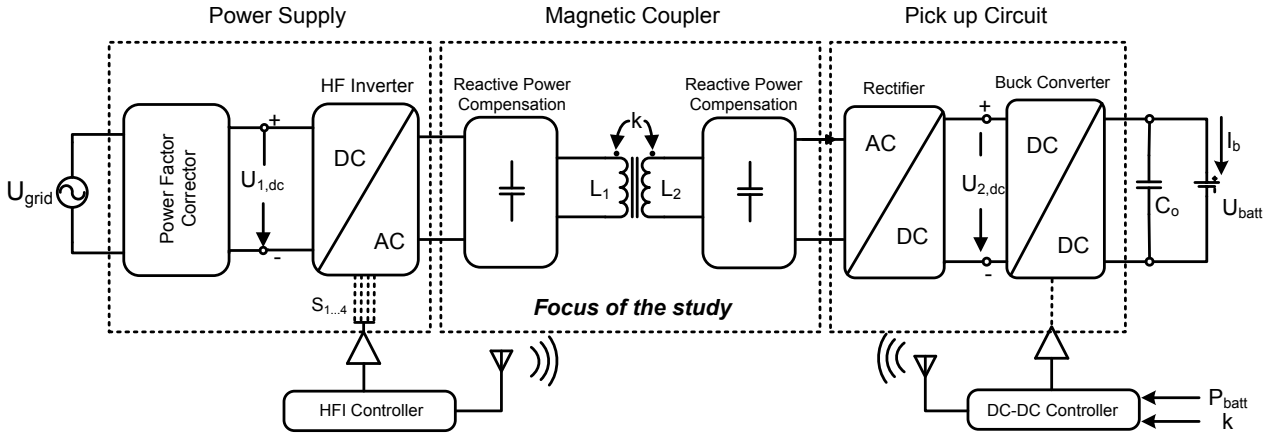

Fig. 1. Schematical IPT system overview from the grid to the battery along with the focus of this study.

II. Fundamentals of IPT Systems

A typical IPT system (Fig. 1) for EV charging from grid to battery consists of three power conversion stages: (i) power supply unit consisting of a high frequency inverter coupled with a PFC, (ii) the magnetic stage comprising of the magnetic couplers along with the resonant capacitors, and (iii) the pick-up circuit which contains a rectifier followed by a dc-dc converter controlling the power to the EV battery. The focus of this study is on the magnetic stage as highlighted in Fig 1. Important parameters that are necessary to determine the performance of the magnetic pads are coupling (k), native quality factors (Q_{L}), power densities and maximum possible efficiencies:

$$k = \frac{M}{L_1 L_2} \tag{1}$$

$$Q_{\mathrm{L}} = \frac{\omega L}{r_{\mathrm{ac}}} \tag{2}$$

$$r_{\mathrm{ac,i}} = \frac{\Sigma P_{\mathrm{loss}}}{I_{\mathrm{i}}^2} \tag{3}$$

$$\mathrm{FOM} = k\sqrt{Q_{\mathrm{L1}} Q_{\mathrm{L2}}} \tag{4}$$

$$\alpha = \frac{P_{\mathrm{out}}}{A_{\mathrm{coil}}} \tag{5}$$

$$\gamma = \frac{P_{\mathrm{out}}}{m_{\mathrm{coil}}} \tag{6}$$

(1) is used to measure the coupling co-efficient between the chargepads where M is the mutual inductance, and L_1,L_2 are the inductances of the chargepads. The native quality factors of the pads are shown in (2), where r_{ac} is the ac resistance of the pads as computed in (3). The figure of merit (FOM) of an IPT system is computed using (4). The area power density and gravimetric power density of the pads are calculated using (5) and (6) respectively.

Since the focus of this paper is on evaluating the pad sizes with different nominal airgaps, the coupling factor is an extremely important design factor. High coupling factor leads to lower pad driving currents which in turn results in lower losses and higher efficiencies. As the figure of merit (FOM) equation suggests, for the same performance an IPT system with high coupling factor k can have lower pad native quality factors which results in lower material usage and sizes. As nominal airgap increases, pads need to be oversized to maintain high values of the FOM. Therefore, it is necessary to establish the scaling laws between optimal size of the chargepads and the nominal power transfer airgap. In the next section, the modeling of the electromagnetic behavior of the chargepads will be presented.

III. Modeling of IPT Coils

Modeling of the electromagnetic performance of the IPT charge pads will be presented in this section. To model the charge pads, 3D Finite element (FE) modeling is used. To extract the magnetic field distribution COMSOL is used and the losses incurring in the couplers are computed by post-processing the data in MATLAB.

A. Axi-Symmetric 3D Finite Element Modeling

A 3D FE model is developed in this section for calculation of the IPT system parameters. The litze wire DD winding is modeled as a rectangular multi-turn coil domain in the model with uniform current density in the cross-section. This reduces the computational load since it will not compute the eddy current losses in the winding. These approximations are valid in this model since the litze wire strand diameter is chosen lower than the skin depth of copper at the operating frequency 85 kHz.

To increase the magnetic coupling of the coils, ferrite bars are added to the design. The core is modeled with a linear or constant relative permeability of $\mu_r = 2400$ to resemble that of material 3C-90. The conductivity of the core material is low ($\sigma = 0.2$ S/m) and therefore eddy currents in the core are neglected, unlike the aluminum shields.

The unbounded space around the coils is bounded by a sphere with radius equal to five times the length of the charge pads so that the accuracy of the simulations is independent of the size of the sphere. Magnetic shielding boundary condition is applied to the bordering surfaces of the sphere. Physics-based automated meshing techniques are used to mesh the

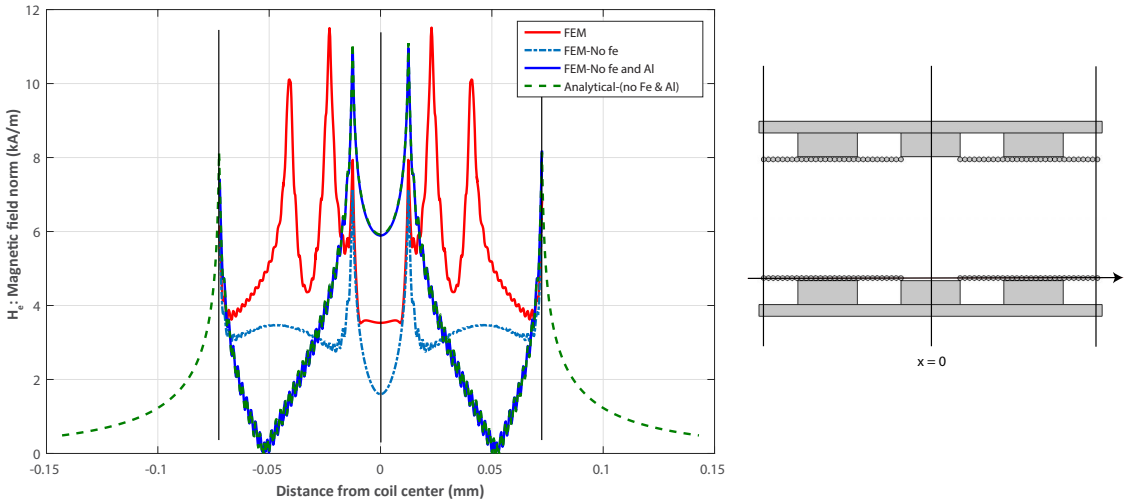

Fig. 2. The variation of external magnetic filed intensity (H_e) penetrating turns of the transmitter coil (lower coil in the adjacent figure).

entire geometry. For accurate computation of the eddy currents and the stray fields, dense meshing is used in the aluminum shields with a maximum mesh size of one-third of the thickness of the aluminum shield. FE modeling is time-consuming, especially when used for optimization purposes. To reduce the computational load, axial symmetries of polarized DD coils are exploited as highlighted in Figure 3. This concludes the 3D FE modeling of the IPT couplers. The computation of losses will be presented in the next section.

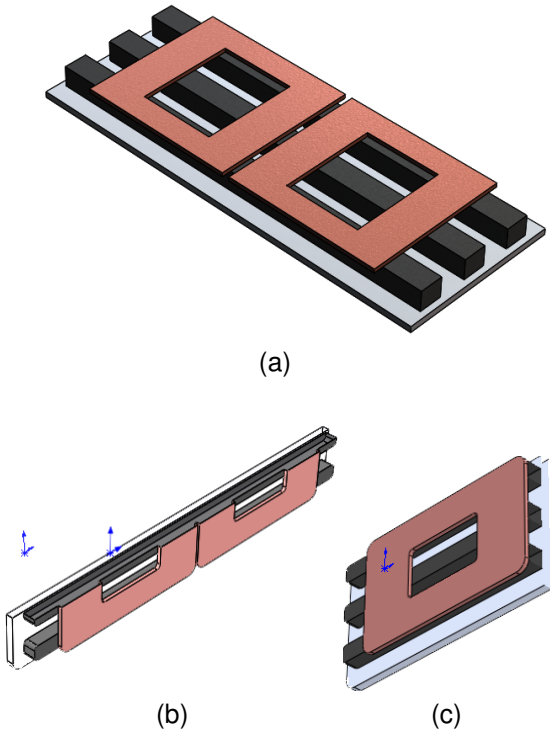

Fig. 3. Axi-symmetric FE modeling of polarized DD couplers: (a) a full DD coil, (b) axis of symmetry along the ferrite strip where magnetic insulation boundary condition can be used since the coil currents are perpendicular to the plane of symmetry, (c) axis of symmetry between the two coils where perfect magnetic conductor boundary condition can be used since the coil currents are parallel to the plane of symmetry. This reduces the computation load by four times.

B. Computation of Losses

The type of losses incurred in the above IPT system are mainly: (a) copper losses in litze wire (ohmic, skin effect and proximity effect losses), (b) core losses in ferrite bars, (c) aluminium shielding losses, and (d) dielectric losses in resonant capacitor banks. Detailed analysis of the individual loss mechanisms is presented in the following:

a) Copper Losses: Copper loss (P_{cu}) is comprised of dc ohmic losses (P_{dc}) and ac losses (P_{ac}) due to skin effect and proximity effect (internal and external). The dc copper loss P_{dc} is computed analytically from the length of the litze wire needed and the resistance per unit length data from the manufacturer's datasheet. It must be noted that in reality, these losses can be higher since the resistivity of copper is temperature dependent which is not considered in this paper due to the lack of a thermal model. The ac losses are computed using the following equations:

$$P_{\text{skin}} = n.r_{\text{dc}}.F_R(f_0).\left(\frac{\hat{I}}{n}\right)^2.L_{\text{coil}} - P_{\text{dc}} \tag{7}$$

$$P_{\text{prox,int}} = n.r_{\text{dc}}.G_R(f_0).\frac{\hat{I}^2}{2\pi^2 d_a^2}.L_{\text{coil}} \tag{8}$$

$$P_{\text{prox,int}} = \sum_{i=i}^{N} n.r_{\text{dc}}.G_R(f_0)\int_{l_i}\hat{H}_{\text{e}}(l)^2 dl \tag{9}$$

where n denotes the number of strands in the litze wire, r_{dc} is the dc resistance per unit length of unit strand of the litze wire, $\hat{H}_e$ is the external magnetic field penetrating the individual coil turns, $F_R(f_0)$ and $G_R(f_0)$ are frequency dependent factors

detailed in [9]. For accurate loss estimation, $\hat{H}_e$ is extracted from a 2D FE model data separately for each turn and summed over for all the N number of turns as shown in Figure 2. It can be seen from the plot that the external magnetic field $\hat{H}_e$ penetrating the coils increase manifold due to the proximity of the ferrite strips. It can also be extracted directly from the 3D model. However, it underestimates the $\hat{H}_e$, since a multi-turn coil domain is used in the 3D FE model.

b) Core Losses: The ferrite core losses (P_{fe}) are computed using the Steinmetz equation and integrating it over the core volumes:

$$P_{\text{fe}} = \iiint_V \kappa f_0^{\alpha} \hat{B}^{\beta} dV \tag{10}$$

where the Steinmetz parameters of the core material 3C-90 are $\kappa = 3.2\text{E-}3$, $\alpha = 1.46$ and $\beta = 2.75$.

c) Aluminium Losses: Compared to the thickness of the aluminium plate the skin depth of aluminium at an operating frequency of 85 kHz is smaller. Therefore, an Impedance Boundary condition is used in the 3D FE model which sets the skin depth to zero, making all induced currents flow on the surface of the conductors. Mathematically, the relation between the magnetic (**H**) and electric field (**E**) at the boundary reads:

$$\mathbf{n} \times \mathbf{H} + \sqrt{\frac{\epsilon - j\sigma/\omega}{\mu}} \mathbf{n} \times (\mathbf{E} \times \mathbf{n}) = 0 \tag{11}$$

The distribution of the dissipated power, P_d (SI unit: W/m^2) can be calculated from:

$$P_d = \frac{1}{2}(\mathbf{J}_S.\mathbf{E}^*) \tag{12}$$

where $\mathbf{J}_S$ is the induced surface current density, and the asterisk (*) denotes the complex conjugate. The overall aluminium eddy losses (P_{al}) are computed by an area integral of the dissipated power (P_d) over the surface of the aluminium shield.

d) Capacitor Dielectric Losses: Polypropylene film capacitors from KEMET are considered for resonant compensation due to their relatively low dielectric losses [10]. The dielectric loss factor $\tan\delta$ is chosen to be 0.2% at 100kHz. For safe operation, capacitors are divided into arrays to satisfy the voltage and current ratings of the individual capacitors. The capacitor dielectric loss is estimated according to

$$P_{\text{cap}} = \frac{\tan\delta(f)}{\omega C} I_{\text{rms}}^2 \tag{13}$$

Finally, the total loss (P_{loss}) of the system is computed by summing the above losses and therefore the efficiency of power transfer (η). The ac resistance of the couplers are derived as following:

$$r_{\text{ac,i}} = \frac{P_{\text{cu,i}} + P_{\text{al,i}} + P_{\text{fe,i}}}{I_{\text{i}}^2} \tag{14}$$

where i denotes either primary or secondary pad and I_{i} is the driving current for that pad. It must be noted that, since $r_{\text{ac,i}}$ denotes the ac resistance of the IPT couplers the capacitor dielectric loss (P_{cap}) is not included there.

This concludes the FE modeling of the IPT couplers along with an the analytical formulae used to estimate the different loss mechanisms incurring in the pads. To investigate the effect of coupler sizes on the losses and the efficiency of power transfer, a optimization framework will be presented.

IV. Multi-Objective Optimization Framework

In the previous section, detailed IPT coupler modeling strategy is discussed. The models developed are used in this section to build an optimization framework for the IPT couplers. This section consists of two sub-parts: (a) optimization details: which includes the optimization targets, variables and the constraints, and (b) system analysis: where the steps needed to evaluate a single IPT coupler design are discussed.

TABLE I
IPT system specfications

Symbol	Description	Value
δ	Operational air-gap	50, 100, 250, 400 mm
P_{out}	Battery power requirement	5 kW
f	Operational frequency	85 kHz
U_{batt}	Nominal battery voltage	400 V
$U_{1,\text{dc}}$	Input dc link voltage	750 V
$U_{2,\text{dc}}$	Pick up dc link voltage	400-750 V

A. Optimization Search Space, Targets, and Constraints

All geometrical parameters of coupler structure as shown in Fig. 4 are considered as optimization variables. The range of the variables is chosen to be wide enough to allow the particle swarm optimization (PSO) algorithm to consider any feasible design. Table II presents the description and range of all the optimization design variables.

The goal of this paper is to derive the relationship between coupler sizes and nominal airgap. Therefore, it is important to build a framework to derive the scaling laws between them. With increasing airgap, the inter-pad coupling reduces which in turn leads to reduction of power transfer efficiency. Therefore, regardless of airgap a good power transfer efficiency is required. To that end, three optimization targets are chosen:

1) Maximize dc-dc efficiency (η)
2) Maximize gravimetric power density (γ)

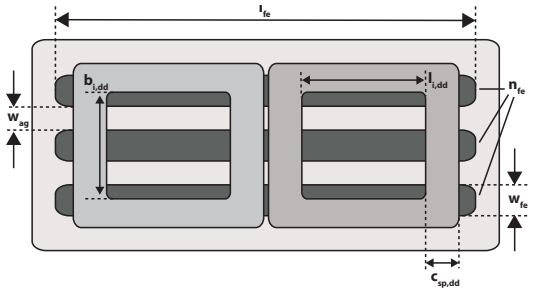

Fig. 4. Design variables for DD primary and secondary pad topology. In both figures, the ferrite thickness (h_{fe}) is a variable which is not shown. The coil spread parameter (C_{sp}) is defined as: $C_{\text{sp}} = N \times d$, where N is the number of turns and d is the external diameter of the litze wire which depends on the number of strands (n_{str}).

TABLE II
OPTIMIZATION VARIABLES AND RANGE

Variables	Description	Range
N	Number of turns	5 - 50
n_{fe}	Number of ferrite strips	1-7
$l_{\text{i,dd}}$	Inner length of the dd coil	10-35 mm
$w_{\text{i,dd}}$	Inner width of the dd coil	10-35 mm
w_{fe}	Width of the ferrites	5-25 mm
h_{fe}	Thickness of ferrites	5-35 mm
l_{fe}	Length of ferrite strips (%)	20-120%
w_{ag}	Air gap between ferrite strips(%)	20-80%

3) Maximize receiver pad area power density (α)

Table I shows the IPT system specifications for which the optimization is carried out. Specific constraints are put on the optimization solution space to ensure feasible and interesting designs. A global limit of 90% efficiency is put on all the designs at different air gaps. A hard limit of 5A/mm^2 is placed on the litz wire current density to ensure thermal stability. To avoid bifurcation phenomena (multiple operating modes), limits on coil quality factors are placed by following bifurcation criterion proposed in [11]. The maximum flux density in the ferrite cores is set to be 0.45 T (saturation flux density for 3C-90 core material). Coil designs which violate the above constraints are removed from the repository.

Few augmentations on the basic algorithm are discussed below. *(1) Multi-objective PSO:* The original algorithm can only be used for single objective optimization. This is undesirable for the IPT optimization since trade-offs between power densities and efficiencies need to visualize. To that end, the single objective algorithm is modified to work with multiple conflicting targets simultaneously [12]. This is realized by storing Pareto optimal solutions in a repository and picking the global best target randomly from this repository. This leads to a larger exploration of optimization space at the cost of more time required to obtain the optimal designs. To prevent unnecessary exploration of undesirable *(2) Handling boundary constraints:* The basic PSO algorithm has no provision for restrictions on variables. However, such requirements are needed in any engineering optimization problem to ensure realistic designs. In literature, several approaches are presented to handle design particles outside the search space. In this paper, an approach based on placing particles on the border of the search space using a combination of variable clipping and reflecting [13].

B. System Analysis

The models developed in section III are used here to analyze a singular IPT design. Figure 5 presents the entire system analysis step by step. There are three main performance parameters: (a) efficiency, (b) gravimetric and area related power density and stray field. The stray magnetic field generated by IPT couplers should comply with the guidelines set by ICNIRP [14]. It stipulates that the general public should not be exposed to RMS magnetic flux densities greater than 27 µT (100 µT for occupational exposure). In this paper, it is measured at 300 mm from the receiver coil center in the vertical direction [5]. This concludes the overall system

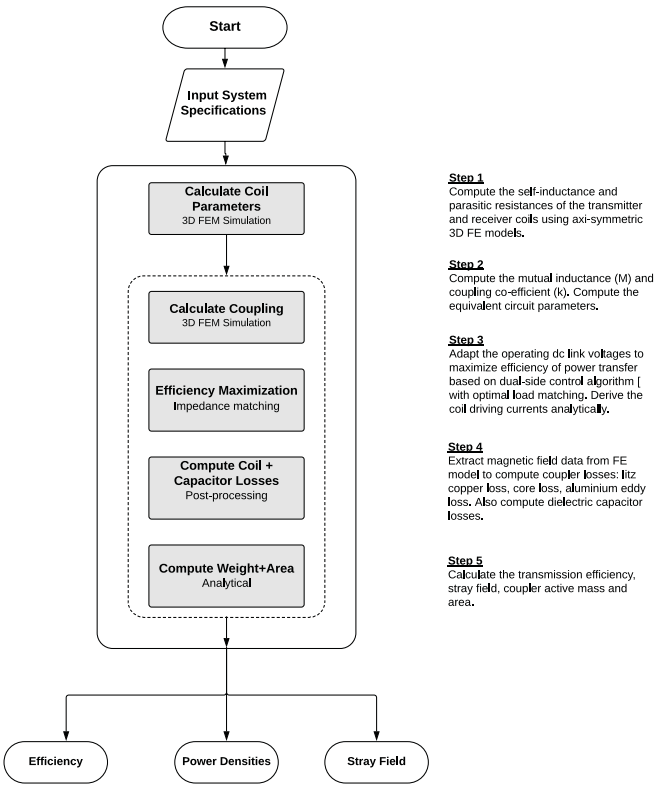

Fig. 5. System analysis of a single IPT coupler system design during the optimization run.

analysis and the optimization framework. The results are presented in the next section.

V. RESULTS

The results of the multi-objective optimization are presented and discussed in this section. The Pareto fronts showing the trade-offs between efficiency and power densities are compared for the four different air gaps. From the different air gap fronts, particles or designs are selected which has the same power transfer efficiency. The approximate scaling laws are derived based on the evolution of the sizes of the selected designs.

A. High-level results

Fig. 6a and Fig. 6b show the side views of the 3D Pareto optimal front which highlights the trade-offs between efficiency and the power densities. Based on the figures, some observations are drawn below:

- The gradient of the Pareto fronts: $\eta-\gamma$ and $\eta-\alpha$ are very sensitive to the nominal air gap as shown in Figure 6a and Fig. 6b.

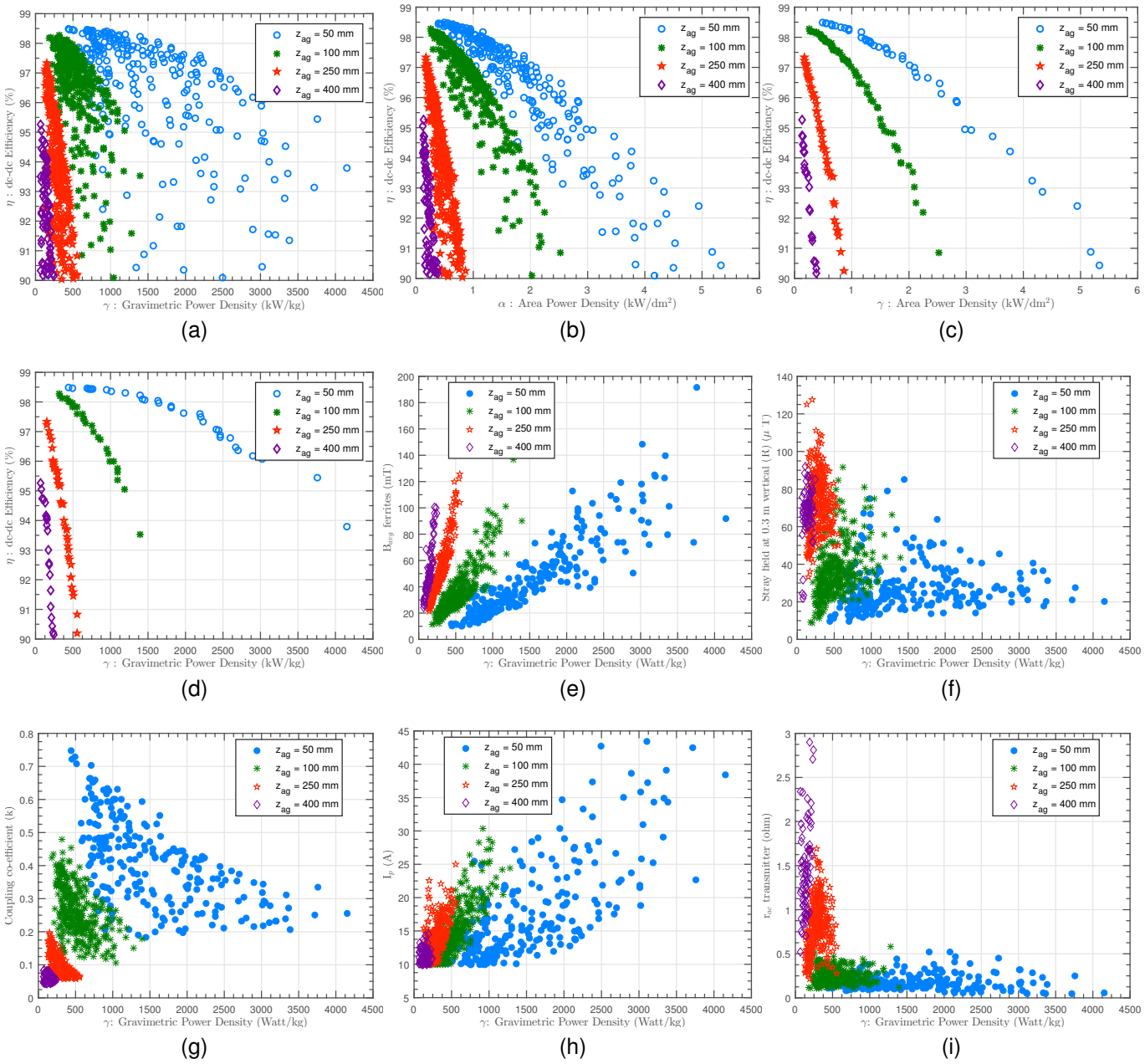

Fig. 6. The trade-offs between efficiency and power densities for the four different air-gaps are shown in side view 2D Pareto representation of (a) $\eta - \gamma$ (b) $\eta - \alpha$. The sub-fronts of the same are highlighted in (c) and (d). The sharp decline of the $\eta - \gamma$ and front $\eta - \alpha$ fronts with increasing air gaps is evident. (e) shows the variation of the average flux density in the ferrite strips of the chargepads with increasing γ at different air gaps. The computed stray field in the vertical direction is shown in (f). At higher air-gaps, the stray fields can easily go above the 27 µT and/or 100 µT mainly due to higher pad driving currents as shown in (i). (g) shows the coupling co-efficient (k) of the optimal machines at different air gaps. Finally, (h) presents the ac resistance r_{ac} of the transmitter pads. As the air gap increases, the ac resistance of the optimal chargepads increases exponentially.

- The average flux density of the ferrite strips of the charge pads are shown in Fig. 6e. It can be observed that at different air gaps the same flux density is achieved at a lower power density. This can be explained since the pad driving currents are higher at higher air gaps due to lower coefficient of coupling.
- The computation of the stray flux density is presented in Fig. 6f. For a single air gap, it can be seen that the stray field increases approximately linearly with power density. It makes sense since the driving currents are higher with lower coupling coefficient associated with high power density pads.
- The inter-pad coupling coefficient k of the optimal charge pads are shown in Fig. 6g. It can be observed that with increasing air gaps, the coupling reduces drastically. This is due to the addition of twice the extra air gap to the

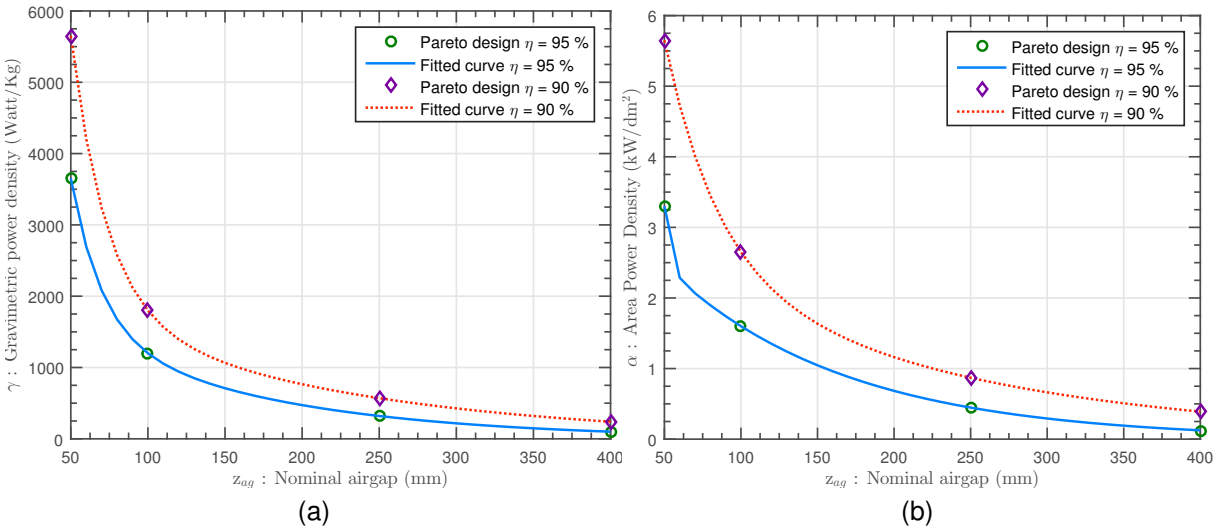

Fig. 7. Relation between (a) γ of optimal chargepads with the nominal air gap and (b) α of optimal chargepads with the nominal air gap . The plots are for different power transfer efficiencies 95% and 90%. An exponential function in the form: $y = ae^{bx} + ce^{dx}$ is used to fit the power density and air gap data. A perfect fit shows that there is indeed an exponential relationship between optimal pad sizes and the nominal air gap.

reluctance path of the linking flux between the couplers. The coupling also reduces with increasing power densities since a lower amount of ferrite material and copper is available to shape the flux.

- The reduction of coupling with increasing air gap leads to one logical consequence: the increase of the pad driving currents for the same amount of power transfer as highlighted in Fig. 6h. It also can be seen from the same figure that there is a lower hard limit of the pad driving currents irrespective of the air gap. This is due to the limit on the receiver circuit dc link voltage ($U_{2,\mathrm{dc}}$) as highlighted in Table I.
- Finally, the ac resistance of the Pareto optimal charge pads (r_{ac}) are shown in Fig. 6i. The figure depicts a sharp increase as the power transfer gap increases. This can be explained by the following reasons: (a) to achieve similar coupling co-efficients the amount of copper and ferrite material needed in much more for designs catering to larger air gaps (see Fig. 6g) which intrinsically leads to higher dc resistance and ac resistance (due to higher proximity losses in litze wires due to increased ferrite material) of the pads, (b) the increased driving currents lead to higher average flux density in the ferrite strips which increases the core losses by an even higher factor (β = 2.75) as shown in the Steinmetz equation (10).

This concludes the general analysis of the optimization results. In the following section, this result will be used to derive approximate scaling laws for IPT charge pads with nominal airgaps.

B. Derivation of Scaling laws

The goal of this paper is to investigate the relationship between optimal pad sizes and the nominal air gap. To that end, a multi-objective optimization framework has been built to generate non-dominated Pareto optimal designs which deliver the highest possible efficiency at a given power density (γ or α). In this section, these Pareto designs are analyzed in detail to derive approximate scaling laws. The approach is presented below:

- Approximate quadratic curves are fitted on the $\eta - \gamma$ and $\eta - \alpha$ fronts (Fig. 6d and Fig. 6c).
- Pareto optimal designs from different air gaps are selected at different efficiency levels (95% and 90%).
- Using curve fitting techniques, a curve is fitted through the area power density and gravimetric power densities of these selected designs.

The results of the approach described above are shown in Fig. 7. It shows an *exponential relationship between the nominal air gap and the coupler optimal power densities*.

VI. Conclusion

Determining the size of inductive couplers in IPT EV charging systems is an important and complex task. This is mainly due to varying air gaps and power levels associated with multiple classes of EVs in multiple charging locations. Current methods reported in the literature for selecting coupler sizes rely on rules of thumb and intuition. Such methods are time-consuming, inaccurate and impractical.To that end, this paper determines the relation between the nominal air gap and optimal coil size for polarized couplers using a multi-objective optimization approach. DD couplers are optimized w.r.t power transfer efficiency and power densities at different air gaps ranging from 50 mm to 400 mm. From the resulting Pareto fronts, designs with a similar efficiencies are chosen at different air gaps. Analyzing the power densities of these selected designs the approximate relation between the air gap and coil sizes are derived. The results show an exponential

increase in optimal coupler weight and area with an increasing nominal air gap.

This paper reveals the relationship between optimal coil sizes and nominal air gap. It must be noted that coupler sizing also depends on the amount of required power transfer. Therefore, the power density limits of IPT charge pads may also be decided on the thermal limit depending on the maximum loss density it can dissipate. An interesting direction for future research will include combining the thermal and electromagnetic behavior for high power IPT charge pads.

REFERENCES

[1] K. Van Schuylenbergh and R. Puers, *Inductive powering: basic theory and application to biomedical systems*. Springer Science & Business Media, 2009.

[2] S. Bandyopadhyay, V. Prasanth, L. R. Elizondo, and P. Bauer, "Design considerations for a misalignment tolerant wireless inductive power system for electric vehicle (ev) charging," in *Energy Conversion Congress and Exposition (ECCE)*, pp. 1–10, IEEE, 2017.

[3] G. R. Nagendra, G. A. Covic, and J. T. Boys, "Determining the physical size of inductive couplers for ipt ev systems," *IEEE Journal of Emerging and Selected Topics in Power Electronics*, vol. 2, no. 3, pp. 571–583, 2014.

[4] F. Y. Lin, G. A. Covic, and J. T. Boys, "Evaluation of magnetic pad sizes and topologies for electric vehicle charging," *IEEE Transactions on Power Electronics*, vol. 30, no. 11, pp. 6391–6407, 2015.

[5] R. Bosshard, J. W. Kolar, J. Mühlethaler, I. Stevanović, B. Wunsch, and F. Canales, "Modeling and pareto optimization of inductive power transfer coils for electric vehicles," *IEEE Journal of Emerging and Selected Topics in Power Electronics*, vol. 3, no. 1, pp. 50–64, 2015.

[6] S. Bandyopadhyay, V. Prasanth, P. Bauer, and J. Ferreira, "Multi-objective optimisation of a 1-kw wireless ipt systems for charging of electric vehicles," in *Transportation Electrification Conference and Expo (ITEC)*, pp. 1–7, IEEE, 2016.

[7] G. A. Covic, M. L. Kissin, D. Kacprzak, N. Clausen, and H. Hao, "A bipolar primary pad topology for ev stationary charging and highway power by inductive coupling," in *Energy Conversion Congress and Exposition (ECCE)*, pp. 1832–1838, IEEE, 2011.

[8] G. R. Nagendra, G. A. Covic, and J. T. Boys, "Determining the physical size of inductive couplers for ipt ev systems," *IEEE Journal of Emerging and Selected Topics in Power Electronics*, vol. 2, no. 3, pp. 571–583, 2014.

[9] J. Mühlethaler, "Modeling and multi-objective optimization of inductive power components," 2012.

[10] T. Diekhans, F. Stewing, G. Engelmann, H. van Hoek, and R. W. De Doncker, "A systematic comparison of hard-and soft-switching topologies for inductive power transfer systems," in *Electric Drives Production Conference (EDPC)*, pp. 1–8, IEEE, 2014.

[11] C.-S. Wang, G. A. Covic, and O. H. Stielau, "Power transfer capability and bifurcation phenomena of loosely coupled inductive power transfer systems," *IEEE transactions on industrial electronics*, vol. 51, no. 1, pp. 148–157, 2004.

[12] C. A. C. Coello, G. T. Pulido, and M. S. Lechuga, "Handling multiple objectives with particle swarm optimization," *IEEE Transactions on evolutionary computation*, vol. 8, no. 3, pp. 256–279, 2004.

[13] Y. Del Valle, G. K. Venayagamoorthy, S. Mohagheghi, J.-C. Hernandez, and R. G. Harley, "Particle swarm optimization: basic concepts, variants and applications in power systems," *IEEE Transactions on evolutionary computation*, vol. 12, no. 2, pp. 171–195, 2008.

[14] J. Lin, R. Saunders, K. Schulmeister, P. Söderberg, A. Swerdlow, M. Taki, B. Veyret, G. Ziegelberger, M. H. Repacholi, R. Matthes, *et al.*, "Icnirp guidelines for limiting exposure to time-varying electric and magnetic fields (1 hz to 100 khz).," *Health Physics*, vol. 99, pp. 818–836, 2010.